metals

MDPI

Article

Effect of the Reinforcing Particle Introduction Method on the Tribomechanical Properties of Sintered Al-Sn-Fe Alloys

Nikolay M. Rusin, Alexander L. Skorentsev and Andrey I. Dmitriev *

Institute of Strength Physics and Materials Science of Siberian Branch Russian Academy of Sciences (ISPMS SB RAS), 2/4 pr. Akademicheskii, 634055 Tomsk, Russia; rusinnm@ispms.ru (N.M.R.); skoralexan@ispms.ru (A.L.S.)
* Correspondence: dmitr@ispms.ru

Abstract: The present paper reports the results of the comparative study of mechanical properties of sintered disperse-strengthened Al–40Sn alloy depending on the method of reinforcing particle introduction. The study is performed on two mixtures of aluminum and tin powders: one is admixed with 5.5–14.6 wt% of pure iron powder and the other contains the same amount of iron, but as a component of aluminide Al_3Fe powders. The volume fraction of tin remains unchanged in all mixtures, being equal to 20%, and the concentration of hard particles increases due to a decrease in the volume fraction of the aluminum phase. Green compacts are sintered in the vacuum furnace at a temperature above the melting point of aluminum. The sintered material is a composite containing three phases: α-Al, β-Sn, and Al_3Fe, in which the tin volume fraction is constant. Testing of the sintered composites for compression shows that the addition of finished Al_3Fe particles has a more beneficial effect on their mechanical properties as compared to the addition of pure iron powders. In the latter case, aluminides are formed during sintering. The ultimate strength of composites reaches 180 MPa. Mechanisms of sintering of composites and the related structure and mechanical properties are discussed.

Keywords: sintered aluminum alloy; mechanical properties; structure; iron aluminides

check for updates

Citation: Rusin, N.M.; Skorentsev, A.L.; Dmitriev, A.I. Effect of the Reinforcing Particle Introduction Method on the Tribomechanical Properties of Sintered Al-Sn-Fe Alloys. *Metals* **2023**, *13*, 1483. https://doi.org/10.3390/met13081483

Academic Editor: Emin Bayraktar

Received: 30 June 2023
Revised: 4 August 2023
Accepted: 14 August 2023
Published: 18 August 2023

Copyright: © 2023 by the authors. Licensee MDPI, Basel, Switzerland. This article is an open access article distributed under the terms and conditions of the Creative Commons Attribution (CC BY) license (https://creativecommons.org/licenses/by/4.0/).

1. Introduction

Aluminum–tin alloys have good resistance to adhesion wear due to the ability of Sn to form a thin inert film on the friction surface [1–4]. The pressure of intensive adhesion of such alloys with hard counterbodies increases with a rise in the content of Sn up to 50 wt% (~25 vol%) [5–7]. At the same time, tin weakens the Al matrix since its thin interlayers are located at the aluminum grain boundaries, replacing the strong cohesive Al–Al boundaries with weak adhesive Al–Sn boundaries. For this reason, there is a restriction on the concentration of tin in aluminum, and Al–Sn alloys are used as thin coatings on durable bearing liners (Aluminum antifriction alloys).

The solubility of tin in solid aluminum is low ($\leq$0.2 at %) [8,9]. Due to this feature, nucleation and growth of refractory aluminum grains in cooling melt are accompanied by the pushing of tin atoms on their surface in the form of thin interlayers. As a result, at a high concentration of tin, the interlayers form a continuous net. Hence, it is impossible to decrease the area of weak interfacial boundaries using a rapid cooling of Al–Sn melt of a given composition. Since low-melting tin is not subjected to strain hardening under normal conditions, plastic flow of the Al–Sn specimens under loading is localized in soft interlayers of tin net even at low strain. The plasticity of the tin interlayers is quickly exhausted as they become thinner, resulting in their delamination from the aluminum phase.

If a material with such a structure is subjected to severe mechanical processing, such as extrusion and rolling, accompanied by a strong change in the shape of the grains under the action of high hydrostatic pressure, the solid tin net will disintegrate into separate inclusions. As a result, the mechanical properties of Al–Sn alloys will increase [10,11]. Unfortunately,

such processing significantly reduces the transverse dimensions of castings, making the manufacture of large products difficult and even impossible. The structure of Al–Sn alloys can also be refined by attrition of the powder mixture before its sintering [12,13]. In addition, other approaches can be used to prepare antifriction Al–Sn alloys with a high bearing capacity [14–17]. However, the processing methods employed in these cases are not very productive and require the use of complex and expensive equipment.

The strength of an Al matrix with a high Sn content can also be increased by powder metallurgy methods [18–20]. The enhancing of bearing capacity of sintered Al–Sn alloys is attributable to the fact that at the proper sintering temperature of Al–Sn powder compacts, only some aluminum particles dissolve in liquid tin, while the remaining particles coalesce and form a rigid Al skeleton which is able to resist an external load. It was found that sintered Al alloys with ~40 wt% (~20 vol%) Sn have the maximum wear resistance under dry friction.

Nevertheless, the hardness and strength of the sintered alloys remain low because their sintering temperature is relatively high. Due to this fact, matrix grains located near the friction surface and tin interlayers between them are extended easily in the direction of friction forces and become thinner. As mentioned above, this leads to the depletion of the plasticity reserve of the material in near-surface layers, its cracking, and the formation of hard deformed particles, which increases the wear rate of the friction pair. Therefore, in order to reduce the tendency for localization of plastic flow in Al–Sn alloys, it is necessary to increase the strength of interfacial boundaries. For this purpose, hard particles can be added on the Al boundaries with tin interlayers, which will prevent the relative displacement of the matrix grains. However, not all hard particles are suitable for these purposes, only those that are well wetted by both tin and aluminum [21–24] and do not form brittle transition layers at the interfaces with these metals [25]. Saturated transition metal aluminides of the Al_3Fe type are among such materials and can be added into the powder mixture as a finished product or prepared directly during sintering of compacts from the elemental Al, Sn, and Fe powders [24]. The last method of introducing hard particles is simple to implement, and mixtures of plastic metal powders are easier to compact, but the result of sintering is not entirely clear since the Al–Sn–Fe ternary system remains poorly studied [25,26].

The aim of the present work is to compare the effects of each method for adding hard iron aluminides on the strength of a sintered Al–40Sn composite.

2. Materials and Methods

The sintered Al–40Sn alloy was chosen as the base for the studied materials because it has the maximum wear resistance under dry friction [18]. It was prepared by sintering a mixture of commercial elemental fine powders of Al (grade ASD-4) and Sn (grade PT 2) in a vacuum furnace. In the present work, the Al–Sn alloy is reinforced with iron, which is added into the powder mixture before sintering either as the pure Fe powder (grade PZh-4) or as the Al_3Fe powder. The Al_3Fe powder is prepared by ball milling small pieces of the material synthesized by high-temperature sintering of a mixture with the atomic composition 75Al-25Fe. Milling is carried out for 4 h at the ball-to-powder weight ratio 20:1. Composites prepared by the first method are referred to as "Ce", and those obtained by the second method are denoted by "Cs". Compositions of the raw mixtures and their phase composition after sintering are enumerated in Table 1. From the tabulated data, it is seen that the volume fraction of iron aluminide Al_3Fe into the sintered composites increases from 13 to 36% due to the reduction in the proportion of the aluminum phase, while the content of tin remains constant at ~20%.

The resulting powder mixtures are compacted into disks 20 mm in diameter and 10 mm in height with a porosity of 5–8%. The powder compacts are sintered in the SNVE vacuum furnace at the residual atmospheric pressure 10^{-2} Pa. The final sintering temperature is 710 °C, and the holding time is 1 h.

The phase composition of the sintered alloys is studied using a DRON-7 diffractometer with CoKα radiation without a monochromator in the symmetric reflection mode. The

scanning angle 2θ varies from 25 to 165° in 0.05° increments. The results are processed by using the PDWin 2.3 software (Burevestnik, Russia, (https://www.bourevestnik.ru, accessed on 17 July 2023).

Table 1. Composition of the powder mixtures sintered in a vacuum at 710 °C (1 h).

Alloy Number	Ce, wt%	Cs, wt%	Al_3Fe/Sn, vol%
1	Al–5.5Fe–38.0Sn	Al–13.5FeAl_3–38.6Sn	13.3/20.0
2	Al–6.9Fe–38.3Sn	Al–17.0FeAl_3–38.2Sn	17.1/19.9
3	Al–9.5Fe–38.0Sn	Al–23.5FeAl_3–37.7Sn	24.2/20.0
4	Al–12.1Fe–37.2Sn	Al–29.6FeAl_3–36.7Sn	31.2/20.2
5	Al–14.6Fe–37.2Sn	Al–35.7FeAl_3–36.7Sn	38.3/20.3

Metallographic specimens are prepared by a conventional method. At first, the specimen surface is ground with sandpaper with a decreasing grit size and then cloth-polished with diamond paste containing abrasive particles less than 1 μm in size. The procedure ends with etching of the polished surface in a 4% solution of nitric acid in alcohol. Structural studies of specimens are performed under an optical microscope and LEO EVO 50 scanning electron microscope (Karl Zeiss, Oberkochen, Germany) equipped with a microanalyzer, which were provided by the shared use center Nanotech of the Institute of Strength Physics and Materials Science SB RAS (ISPMS SB RAS, Tomsk, Russia).

The sintered compacts are subjected to additional pressing in a closed die at a pressure of 300 MPa and a temperature of 250 °C. The press mold in which green compacts were formed is used as a closed die. Out of the resulting compacts, we cut specimens of the size 10 × 5 × 5 mm for compression tests using an Instron-1185 machine (Switzerland). The crosshead speed is 0.5 mm/min. The flow stress of the specimen is calculated by the formula $\sigma_{real} = \sigma(1 - \delta) = \sigma(h/h_0)$, which accounts for the increase in the cross-sectional area of the compressed specimens, where $\delta = \Delta h/h_0$ is the relative deformation of the compressed specimen with the initial height h_0. The measurement error for σ is ±0.2 MPa. Compression tests are stopped when the specimens are fractured or their flow stress is sharply reduced.

The tribological tests were carried out using a tribotester (Tribotechnic, Clichy, France) according to the scheme pin-on-disk without lubrication. The friction surface of the specimens (pins) was 2 × 2 mm. A counterbody (disk) with a hardness of 48 ± 2 HRc was prepared from the structural steel 40H (AISI 5140 steel), which is often used for wear-resistant crankshafts in different machines and mechanisms. The sliding speed was 0.6 m/s, and the pressure on the friction surface was 5 MPa.

3. Results and Discussion

The structure images of green compacts No. 2 reinforced with particles of iron aluminide Al_3Fe (Cs2) or with iron particles (Ce2) are shown in Figure 1a,b. Tin particles (white) are seen to have the form of isolated inclusions, regardless of the compact composition. Iron aluminide particles (gray) are much finer and more uniformly distributed in the compacts as compared to iron particles (blue). In this case, the Al_3Fe particles often border on the Sn particles because the average distance between them in the mixture Cs2 is much less than the distance between the iron and tin powders in the mixture Ce2.

The images given in Figure 1 also reveal that at the same atomic concentrations of Al, Sn, and Fe in the green compacts, the volume fraction of Al_3Fe particles significantly exceeds the fraction of iron particles. This is because each iron atom in the lattice of Al_3Fe compound is surrounded by three aluminum atoms. For this reason, the relative volume fraction of aluminum powders in initial mixture Cs2 is less than in mixture Ce2, and the density of iron-containing hard particles on their surface is higher at the same number of iron atoms in both composites. As a consequence, regions composed only of tin and aluminum powders are rare and small in size in the compact Cs2, while analogous regions

free of hard particles are large in the compact Ce2. These regions consist of a large number of small Al particles which are in contact with each other (Figure 1b).

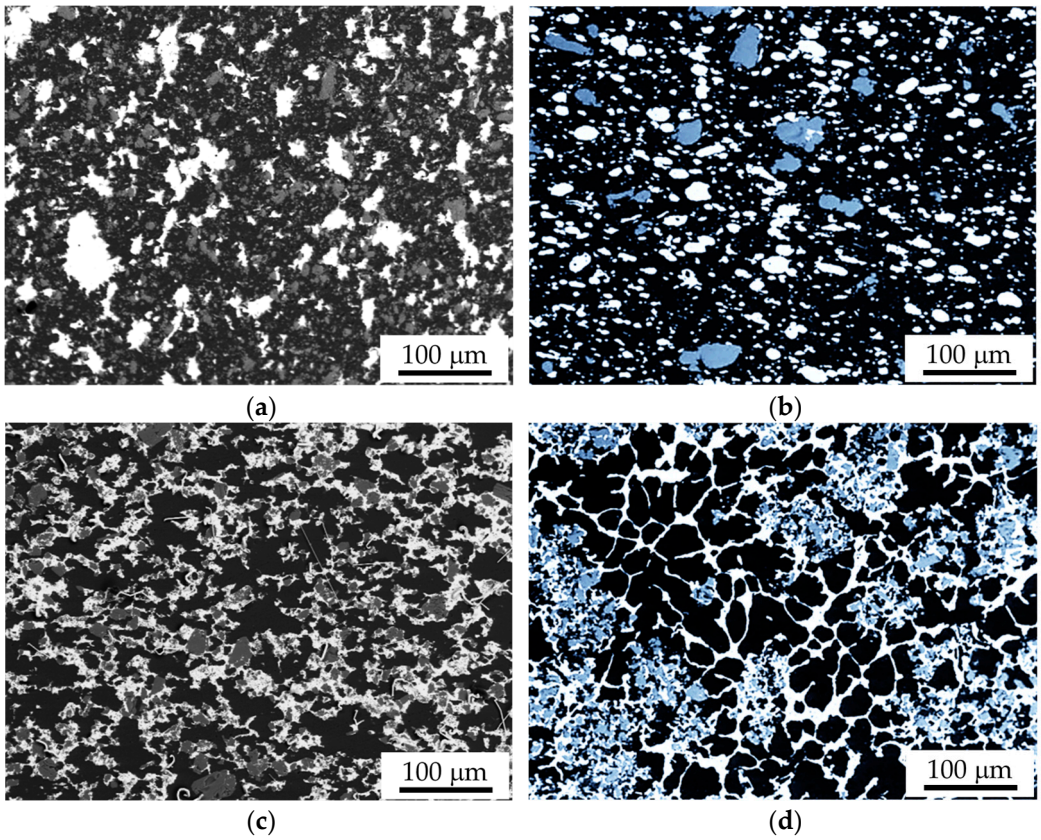


Figure 1. Structure of Cs2 and Ce2 alloys before sintering (**a**,**b**) and after sintering at 710 °C (1 h) (**c**,**d**), respectively.

When raw compacts are heated, Sn powders are the first to melt at a temperature of 232 °C, but the tin melt does not spread over the surface of aluminum particles, since they are covered with an oxide film that is poorly wetted by liquid tin. Such films are always present on aluminum powders, and their thickness on freshly atomized aluminum powders varies from 50 to 150 Å and continues to grow as their storage life increases. Oxide films on aluminum are usually amorphous and hydrated by absorbed water vapor; however, they crystallize upon annealing above 350 °C [27]. Liquid tin penetrates the film cracks and reaches the aluminum surface. The Sn–Al melt quickly moves along the aluminum grain boundaries dividing Al powders on individual grains, and thus spreads over the compact.

According to the thermodynamic analysis of diffusion in liquid tin [28], Al is completely soluble in liquid tin, and its diffusivity is faster than the diffusivity of either Cu or Zn in liquid Sn and about five times greater than the self-diffusivity of liquid Sn. Rapid diffusion of aluminum atoms in liquid tin results in the rapid growth of aluminum matrix grains by the mechanism of liquid-phase recrystallization. Coarsening of aluminum grains is hindered by insolubility of inert particles in the melt at their boundaries. These alloying processes change greatly the structure of compact Cs2 during its sintering at 710 °C for one hour. Thus, almost all Al_3Fe particles initially located between aluminum powders stay at the aluminum grain boundaries and become surrounded by tin, which separate them from the aluminum matrix (Figure 1c).

The tin-based melt in Ce compacts arrives at the iron particles in a similar way, though more slowly, since the volume fraction of iron powders in the equiatomic raw mixtures is almost four times lower than that of Al_3Fe particles, and the distance to them is larger. Consequently, the aluminum regions located between Fe powders are many times larger.

When tin penetrates into such regions, the matrix grains coarsen by the mechanism of liquid-phase recrystallization; however, iron particles remain at the periphery of these regions.

Iron particles that are in contact with the Sn–Al melt form iron aluminide, since the liquid that wets them contains a high concentration of chemically active Al atoms, which are capable of interacting with the iron surface. In principle, many phases with a different structure and composition can be formed in the "Fe–melt" diffusion zone, but the X-ray phase analysis shows the formation of only three phases in all specimens after the completion of alloying: Al, Sn, and intermetallic compound Al_3Fe (Figure 2). Our results are in good agreement with the data of [25].

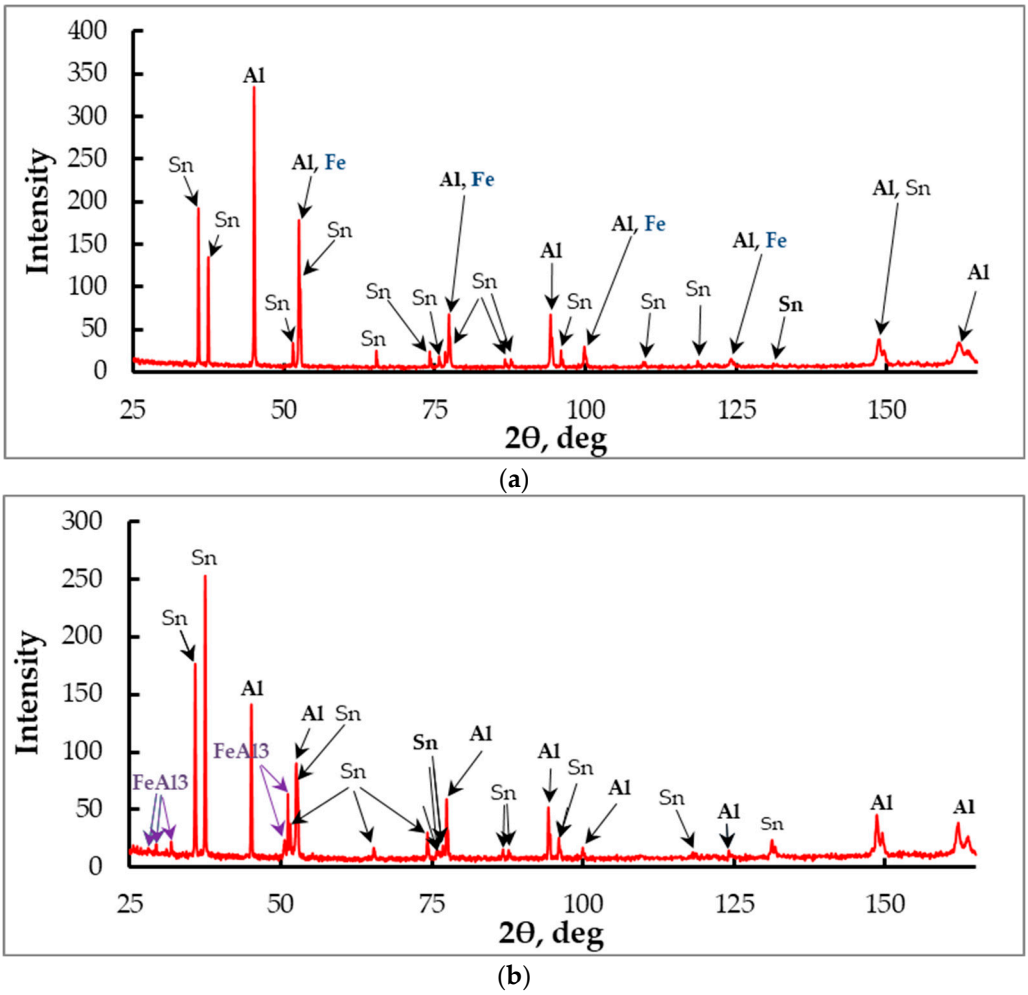


Figure 2. Diffraction pattern of raw (**a**) and sintered at 710 °C (1 h) (**b**) Ce2 alloy.

Diffusion of Al atoms from the melt into iron occurs by the substitution mechanism. Each iron atom in the lattice of the resulting Al_3Fe phase is surrounded by three aluminum atoms. This means that, upon completion of the alloying process in compact Ce2, iron particles are replaced by a new phase with the volume fraction equal to the volume fraction of Al_3Fe particles in alloy Cs2. The lattice parameters of the new phase are very different from those of Fe, which induces stresses in the diffusion zone. These stresses cause cracking of the outer layer of reaction products, which consist of the brittle aluminide phase [29,30].

Since aluminides form in situ, many small particles of Al_3Fe remain at the place of alloying of Fe and Al. The Sn–Al melt that wets iron particles now coats iron aluminide particles and cements them into compact agglomerates. Given the nonuniform distribution of hard Al_3Fe particles in alloy Ce2, even at their high concentration, a significant part of the matrix grain boundaries lacks hard aluminide particles after sintering, and aluminum grains are separated only by tin interlayers (Figure 1d). Aluminum grains quickly coalesce

at places where they contact each other after the heating of compacts above the aluminum melting temperature (large dark regions in Figures 1 and 3). Coarsening of aluminum grains is accompanied by the displacement of the tin liquid to their periphery, where it also cements Al_3Fe particles. The nature of the arrangement of the phases in the prepared alloy is clearly seen in the EDS images obtained in the characteristic beams of the elements (Figure 4).

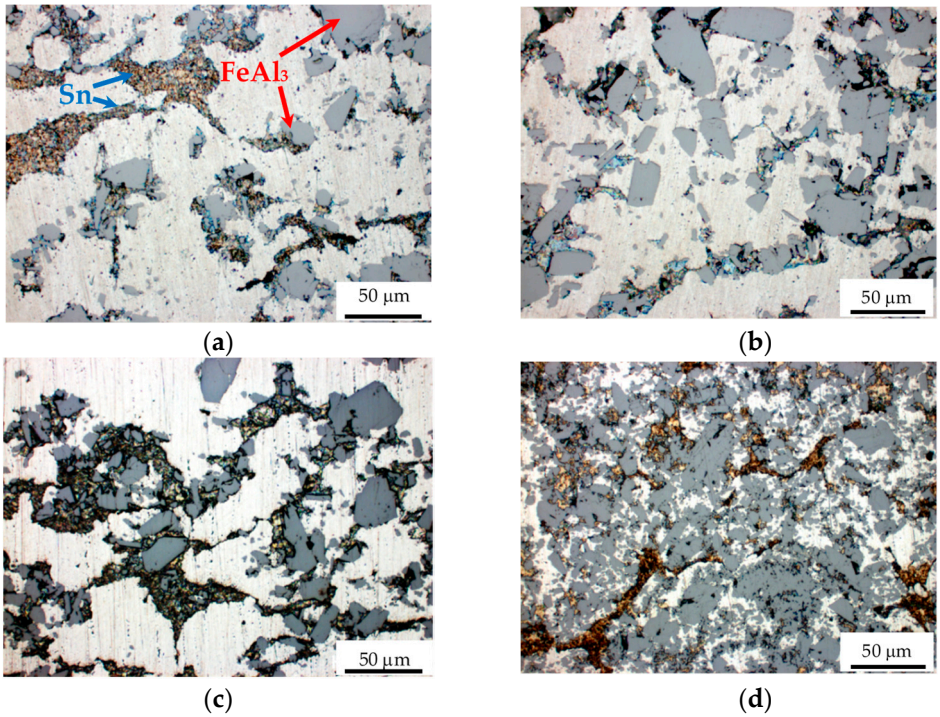


Figure 3. Structure of Ce alloys sintered at 710 °C (1h). Alloy number: 1 (**a**), 3 (**b**), 4 (**c**), and 5 (**d**).

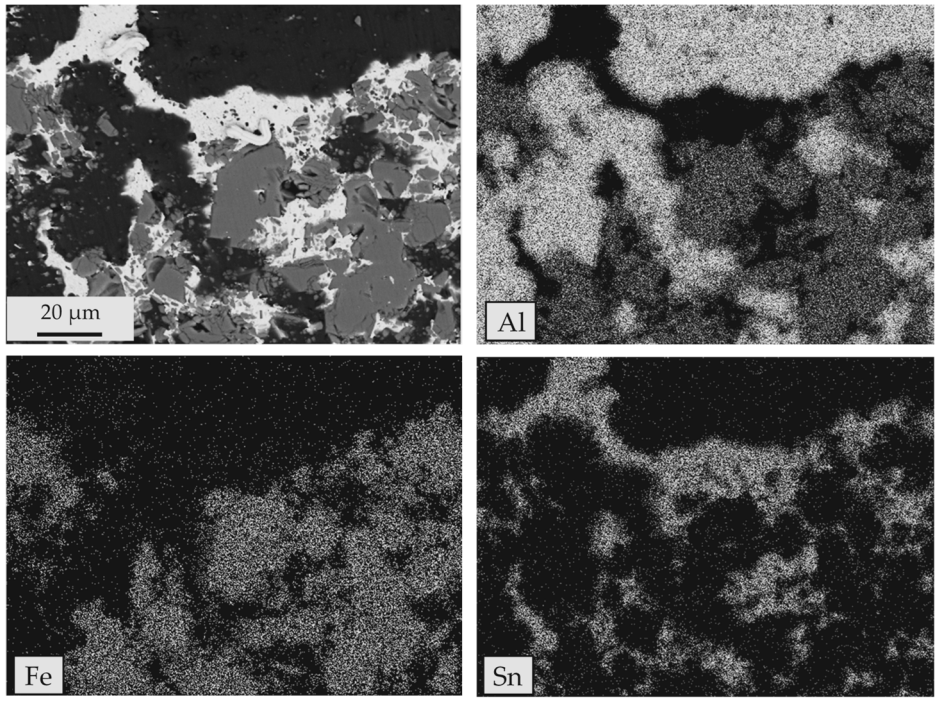


Figure 4. SEM image of the structure of Ce2 alloy sintered at 710 °C (1 h) and distribution map (EDS) of elements over the volume of the alloy.

As for Se alloys sintered from the elemental powder mixture, the increase in the volume concentration of the admixed iron powder is not as fast as the increase in the concentration of Al_3Fe particles (Table 1). Iron is mostly located in interstices of the aluminum powder in the form of individual particles. After alloying with Al, it remains on the periphery of large aluminum regions in the form of agglomerates of fine Al_3Fe particles cemented with tin (Figures 1d and 3). When the iron concentration is not high and the number of the formed agglomerates is small, they do not eliminate contacts between the aluminum particles they edge. After melting, aluminum particles coalesce, resulting in coarse-grained regions after melt crystallization, which are edged with agglomerates of hard particles (Figure 3a–c). However, when the concentration of iron particles in the sintered mixture is high, the volume of agglomerates of the new particles grows so that the surrounding tin is insufficient to coat all new particles and to separate them from the aluminum particles. Aluminum powders that are in contact with the Al_3Fe particles melt, and liquid aluminum, which has a greater affinity for aluminides, begins to spread over the surface of solid particles, replacing tin and forming new Al_3Fe–Al interfaces with stronger adhesive bonds as compared to the Al_3Fe–Sn interfaces. When liquid aluminum spreads over the aluminide surface, it displaces liquid tin from the agglomerates and acts as a binder for hard particles of iron aluminide. This results in a specific structure of the Al–Sn–Fe composite: particle-reinforced coarse aluminum grains with tin interlayers on the periphery, which also contain Al_3Fe particles (Figure 3d).

It is known that iron aluminides dissolve in liquid aluminum. Therefore, particles inside aluminum regions coarsen during sintering due to the dissolution of small particles and the precipitation of dissolved atoms on the surface of larger ones. In addition to liquid-phase recrystallization, there is another coarsening process, namely aggregation of iron aluminide particles, which reduces the interfacial energy in sintered materials. The described processes of the coarsening of iron aluminides in the aluminum matrix are clearly visible in the image given in Figure 3d.

The composition of the studied alloys changes by increasing the volume fraction of Al_3Fe particles and consequently by decreasing the matrix volume, while the concentration of tin remains unchanged and amounts to ~20 vol% (Table 1). This means that the number of aluminum boundaries decorated with iron aluminide particles and coated with tin interlayers increases with an increase in the number of Cs alloy. Liquid tin interlayers prevent the direct coalescence of molten aluminum grains, such that their growth is possible only by the mechanism of dissolution–precipitation, i.e., it is controlled by the rate of diffusion of aluminum atoms in liquid tin. Hard particles also prevent the aluminum grain boundaries from displacing.

In the case of Cs alloys, numerous small Al_3Fe particles are present at a large number of Al boundaries. With increasing content of hard phase particles, the continuous aluminum matrix refines further and further and gradually degenerates to individual Al inclusions in the tin matrix, reinforced with Al_3Fe particles (Figure 5). Most of the hard particles are also coated with tin and thus separated from aluminum in Cs alloys. It is clearly seen in the EDS images obtained in the characteristic beams of the elements (Figure 6).

The mentioned structural differences in alloys Cs and Ce should inevitably affect the mechanical properties of sintered composites. The results of compression tests are shown in Table 2. From the tabulated data, it follows that the mechanical strength of the sintered Al–Fe–Sn composites increases with an increase in the iron content, regardless of the method of its addition into the sintered samples. Thus, an increase in the volume fraction of iron aluminide by 20% in alloys Ce (Table 1) increases their yield strength $\sigma_{0.2}$ and ultimate strength σ_B by almost 40 MPa. The same increase in the content of hard particles in alloys Cs increases their $\sigma_{0.2}$ by 25 Mpa, while σ_B increases by the same value of 40 Mpa. Thus, the contribution of hard Al_3Fe particles to the strength of the sintered Al–40Sn alloy is determined by their concentration and hardly depends on the method of adding them to the sintered powder mixture.

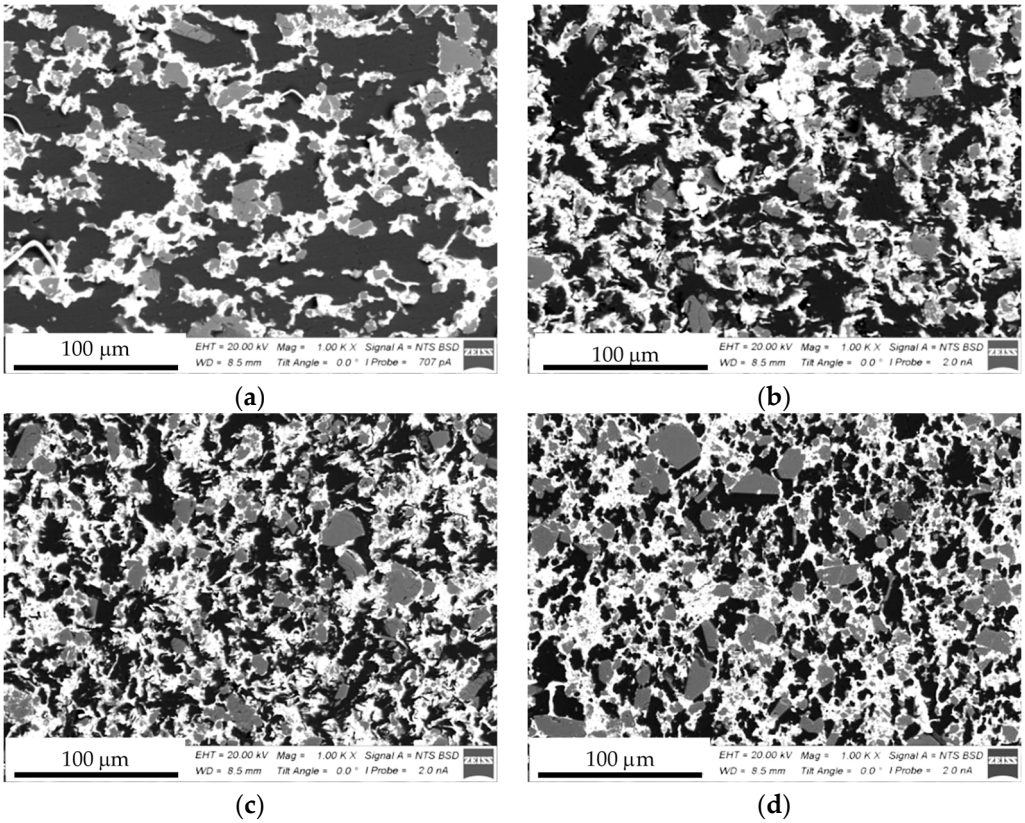


Figure 5. SEM images of the structure of Al–17$FeAl_3$–38Sn (**a**), Al–24$FeAl_3$–38Sn (**b**), Al–30$FeAl_3$–37Sn (**c**), and Al–36$FeAl_3$–37Sn (**d**) alloys sintered at 710 °C (1 h).

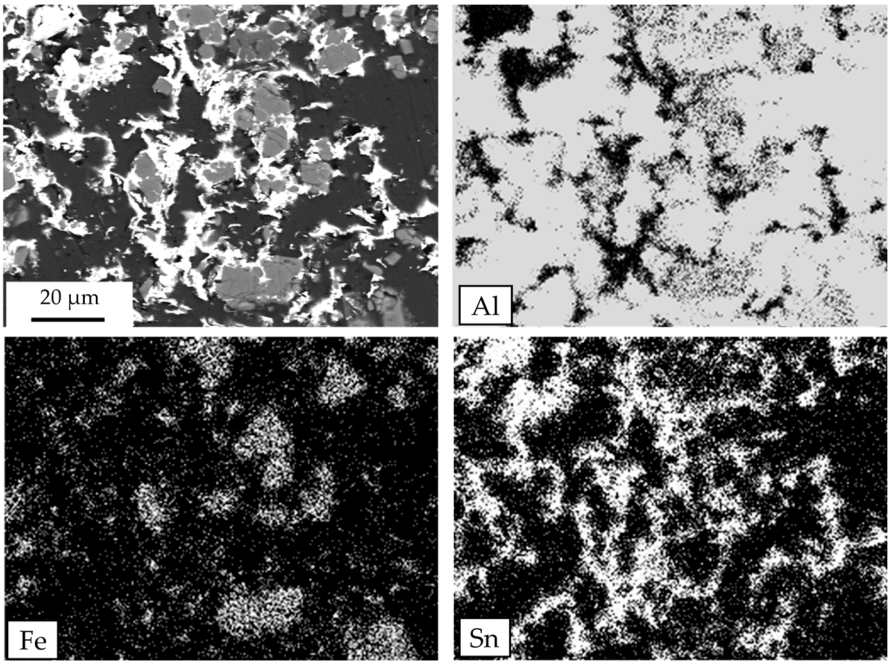


Figure 6. SEM image of the structure of Cs2 alloy sintered at 710 °C (1 h) and distribution map (EDS) of elements over the volume of the alloy.

Since the distance between agglomerates in Ce alloys at low iron content is large, the plasticity of the resulting composites is higher than that of Cs alloys with the same concentration of Al_3Fe particles. With an increase in the iron concentration, the plasticity decreases due to an increase in the volume fraction of hard particles in the composite.

However, this decrease in Cs alloys is relatively smooth, while the plasticity of Ce alloys at the hard particle concentration above 30 vol% decreases sharply. Judging from the structure of such composites (Figure 3d), at the indicated concentrations, tin is displaced from the Sn–Al_3Fe agglomerates and is replaced by aluminum. Simultaneously, Al_3Fe particles come in contact with each other and form a brittle skeleton. The effect of such a skeleton on the plasticity is well illustrated by the stress–strain curves given in Figure 7.

Table 2. Mechanical properties of Al–Fe–Sn composites sintered at 710 °C (1h).

Composition	$\sigma_{0.2}$, MPa	σ_B, MPa	δ(σB), %
Ce2	101	122	≈25
Cs2	109	137	≈17
Ce3	109	134	≈20
Cs3	112	142	≈15
Ce4	118	136	≈4.5
Cs4	120	159	≈15
Ce5	144	165	≈5.5
Cs5	134	179	≈11
Al–40Sn	67	93	≈18

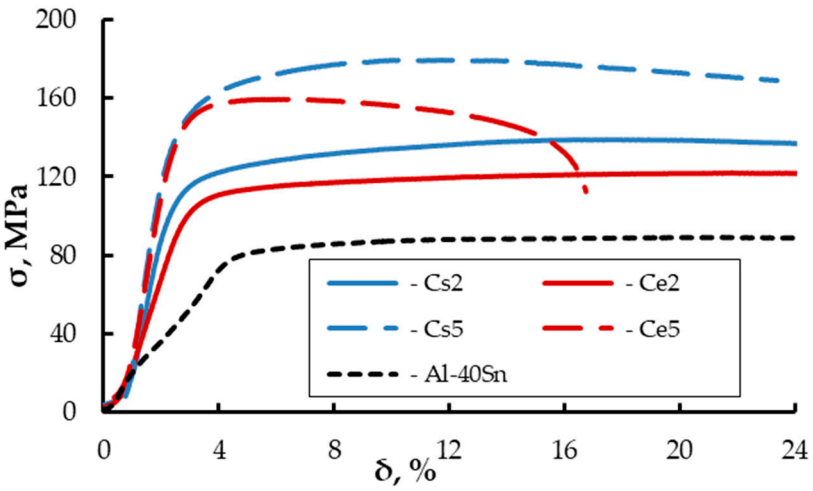
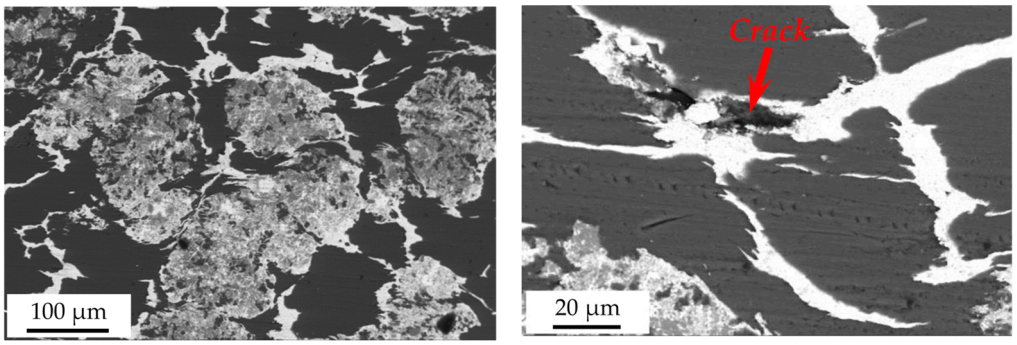


Figure 7. Stress–strain curves of sintered Cs and Ce composites under compression depending on the content of iron aluminides Al_3Fe in them.

It follows from the presented curves that the main increase in the compression strength of the sintered composites occurs at the linear stage of deformation. This stage ends with a sharp knee of the deformation curve, after which the flow stress σ increases insignificantly even at high strain. The flat section of the deformation curve is almost parallel to the ε axis and unambiguously indicates that the deformation of the compressed specimens consisting of the Al, Sn, and Al_3Fe phases—only the first of which is capable of strain hardening under normal conditions—occurs almost without strain hardening of the material. This indicates that the matrix grains hardly experience plastic deformation at this deformation stage, which is due to the deformation localization at the phase boundaries (Figure 8) [26].

Deformation of the sintered specimens proceeds as follows. At the beginning of testing, the added Al_3Fe particles prevent plastic deformation localization, and deformation is uniformly distributed in the test specimen and occurs in all aluminum grains. However, as they are strain hardened, plastic flow localizes along the grain boundaries within the soft tin phase. Thus, the aluminum matrix does not take part in further deformation of the specimen after its rapid hardening at the initial stage of compression. The matrix grains experience only the small deformation necessary to adapt their orientation in such a way as to provide the least resistance to localized shear in the compressed specimen.



(**a**) (**b**)

Figure 8. SEM images of the structure of sintered Ce composite after compression test at low (**a**) and high (**b**) magnification; δ~20%.

This deformation stage with a slight slope, almost parallel to the δ axis, is characteristic of the compression curves of both Al–40Sn alloy and Ce alloy specimens. The higher the concentration of hard particles in the alloy, the shorter this stage. The shortest stage is found in alloys Ce5, which ends with a rapid decrease in the flow stress of the specimens due to material cracking (Figure 8).

At the same concentration of the reinforcing phase, the stress–strain curves of Cs alloy specimens are slightly higher than those of Ce alloys. Even after reaching the plateau, the Cs alloy specimens retain a slight tendency to strain hardening. The positive slope of the deformation curves at this stage is due to the fact that the Al grain boundaries in these composites have more uniformly distributed hard particles, which resist the plastic flow localization in them during compression tests. Whereas in Ce alloys, aluminide particles reinforce not only the boundaries but also the aluminum grains (Figure 3d), preventing them from deforming at a given applied stress. Therefore, deformation in Ce alloys is concentrated in the intergranular space, where nonhardening tin is located. The large size of aluminum grains also contributes to a decrease in the plasticity of Ce alloys.

Preliminary investigation of the influence of reinforcing Al_3Fe particles on the tribological properties of the sintered Al–Sn alloy is carried out on specimens of the sintered Al–40Sn alloy and specimens of alloy No. 2 containing ~17 vol% iron aluminide. It was found that the wear rate of alloy Ce2 is 0.22 μm/m; and for alloy Cs22, its value is 0.19 μm/m. At the same time, the friction coefficient during testing of both alloys is the same and amounts to 0.33. In the case of the Al–40Sn alloy, the wear rate is 0.25, and the friction coefficient is also about 0.3. The friction path of the specimens along the steel counterbody was 1000 m. The composition and structure of the friction surfaces of the specimens and the steel counterbody are analyzed. The pressure and sliding speed of the friction pair are constant. The friction surfaces of the counterbodies are shown in Figure 9, and their chemical composition is given in Table 3.

Table 3. The composition of the friction surface of sintered specimens of the Al–Sn–Fe system shown in Figure 9.

Alloy Composition	Spectrum	Concentration, % at.			
		O	Al	Fe	Sn
Ce2 (Al–6.9Fe–38.3Sn)	Spectrum 1	63.90	23.8	7.8	4.5
	Spectrum 2	60.04	24.3	10.1	4.8
	Spectrum 3	63.83	23.6	8.0	4.5
	Spectrum 4	64.00	22.0	9.3	4.7
	Spectrum 5	65.50	24.0	5.6	4.9
	Spectrum 6	61.86	27.27	5.2	5.7
Al–40Sn	Spectrum 1	59.3	26.3	9.7	4.7

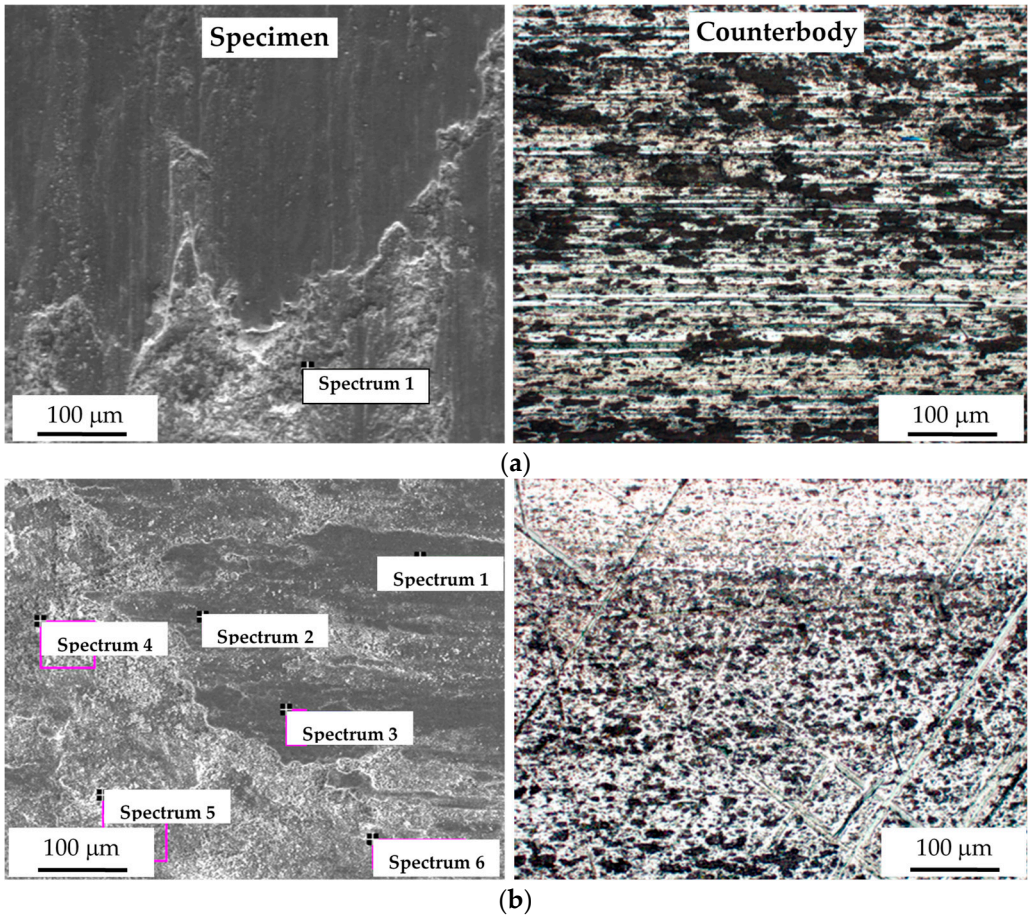


Figure 9. Friction surfaces of samples of alloys Al–40Sn (**a**) and Ce2 (**b**) and the corresponding surfaces of the steel counterbody after a friction path of 1000 m.

It is seen in Figure 9 that iron-containing specimens and specimens of binary composition have similarly structured friction surfaces, on which relatively smooth regions alternate with damaged regions in the form of shallow depressions. These structural elements on the friction surface of the Al–40Sn alloy specimen are larger than those on the surface of the Al–6.9Fe–38.3Sn (Ce2) alloy. Apparently, this is due to the large grain size of the aluminum matrix in the two-component alloy.

The chemical composition of the friction surfaces of the specimens is approximately the same. Its characteristic feature is a high oxygen content and a low concentration of tin (Table 3). Its concentration is about 13% in the sintered specimens, while it is slightly less than 5% on the friction surface. This indicates that a part of the tin is squeezed out of the surface layer and consumed as a solid lubricant; however, its main amount is stored in the mixed surface layer of the tested specimens.

The presence of iron on the friction surface of the Al–40Sn specimen is an unusual result because it is absent in the composition of the sintered alloy. It could be transferred to the specimen surface only from the steel counterbody in the form of microparticles and microchips. Images of the friction paths confirm this suggestion. The steel counterbody surface reveals a large number of scratches parallel to the sliding direction (Figure 9a), whereas there are few scratches on the counterbody surface after contact with the Ce2 specimen (Figure 9b). This indicates that the particles of iron aluminide Al_3Fe in the sintered specimen prevent abrasive wear of the steel counterbody surface during dry friction. Apparently, the hard Al_3Fe particles protruding above the friction surface do not allow harder oxide particles such as Al_2O_3 or SnO to come into frictional contact with the counterbody surface. A rather large amount of these oxide particles form in the mixing layer during its deformation by counterbody asperities. The low wear of the counterbody

surface is also evidenced by the presence of scratches formed randomly, even before the tribological tests (Figure 9b). There are no such scratches on the counterbody surface after contact with the Al–40Sn alloy because its thick layer was worn out. Since the replacement of a worn shaft is expensive, the addition of iron aluminide particles to the antifriction Al–Sn alloy is of practical importance.

4. Conclusions

The analysis of the obtained data suggests the following conclusions.

1. The method of introducing iron aluminides into the Al–40Sn matrix affects their distribution in the sintered specimen: the finished Al_3Fe particles are uniformly distributed along the aluminum grain boundaries, while the same particles synthesized during sintering are arranged into agglomerates, which edge large regions of aluminum grains with tin interlayers.
2. The Al_3Fe particles located at the Al grain boundaries and coated with tin restrain the process of coalescence of aluminum particles during their melting; therefore, Cs alloys with uniformly distributed particles have a finer-grained structure than Ce alloys after sintering under the same conditions.
3. Under compression to a high degree of deformation, sintered specimens with a finely dispersed structure demonstrate better plasticity and strength than specimens of the same composition but with coarse aluminum grains, and therefore reinforcement of Al–Sn powder alloys with finished Al_3Fe particles is more effective than with pure iron ones.
4. The addition of Al_3Fe particles to Al–Sn alloys reduces the abrasive wear of the steel counterbody surface under dry friction conditions.

Author Contributions: Conceptualization, N.M.R. and A.L.S.; writing—original draft preparation, N.M.R.; preparation of the samples, A.L.S.; investigation of the samples, N.M.R. and A.L.S.; substantive revision, A.I.D.; project administration, A.I.D. All authors have read and agreed to the published version of the manuscript.

Funding: This research was funded by the government research assignment for ISPMS SB RAS, project FWRW-2021-0006.

Institutional Review Board Statement: Not applicable.

Informed Consent Statement: Not applicable.

Data Availability Statement: Data sharing is not applicable.

Conflicts of Interest: The authors declare no conflict of interest.

References

1. Bassani, P.; Molteni, M.; Gariboldi, E. Microstructural features and thermal response of granulated Al and A356 alloy with relevant Sn additions. *Mater. Des.* **2023**, *229*, 111879. [CrossRef]
2. Sadawy, M.; Metwally, H.; Abd El-Aziz, H.; Adbelkarim, A.; Mohrez, W.; Mashaal, H.; Kandil, A. The role of Sn on microstructure, wear and corrosion properties of Al-5Zn-2.5Mg-1.6Cu-xSn alloy. *Mater. Res. Express* **2022**, *9*, 096507. [CrossRef]
3. Barros, A.; Cruz, C.; Botelho, T.; Silva, A.; Casteletti, L.; Garcia, A.; Cheung, N. Dry sliding wear features of an Al-20Sn-5Zn alloy affected by microstructural length scales. *Lubricants* **2022**, *10*, 352. [CrossRef]
4. Li, S.; Li, Y.; Guo, H.; Wen, Z.; Zhu, Z. Effect of electromagnetic stirring frequency on tribological performance and corrosion resistance of Al-Sn bearing alloy. *Mater. Today Commun.* **2022**, *32*, 103898. [CrossRef]
5. Bushe, N.A.; Goryacheva, I.G.; Makhovskaya, Y.Y. Effect of aluminum alloy composition on self-lubrication of frictional surfaces. *Wear* **2003**, *254*, 1276–1280. [CrossRef]
6. Mironov, A.E.; Gershman, I.S.; Gershman, E.I. Influence of tin on the tribotechnical properties of complex antifriction aluminum alloys. *J. Frict. Wear* **2018**, *39*, 394–399. [CrossRef]
7. Podrabinnik, P.; Gershman, I.; Mironov, A.; Kuznetsova, E.; Peretyagin, P. Mechanisms involved in the formation of secondary structures on the friction surface of experimental aluminum alloys for monometallic journal bearings. *Lubricants* **2018**, *6*, 104. [CrossRef]
8. Chikova, O.A.; Vyukhin, V.V.; Tsepelev, V.S. Influence of melt superheating treatment on the cast structure of Al–Sn alloys. *Russ. J. Non-Ferr. Met.* **2021**, *62*, 286–292. [CrossRef]

9. Tamura, T.; Li, M.; Takahashi, K.; Inoue, E. Improved solidification structures and mechanical properties of Al–20 wt% Sn alloys processed by an electromagnetic vibration technique. *Mater. Sci. Eng. A* **2023**, *862*, 144416. [CrossRef]
10. Noskova, N.I.; Korshunov, A.G.; Korznikov, A.V. Microstructure and tribological properties of Al-Sn, Al-Sn-Pb, and Sn-Sb-Cu alloys subjected to severe plastic deformation. *Metal. Sci. Heat Treat.* **2008**, *50*, 593–599. [CrossRef]
11. Hernandez, O.; Gonzalez, G. Microstructural and mechanical behavior of highly deformed Al-Sn alloys. *Mater. Charact.* **2008**, *59*, 534–541. [CrossRef]
12. Zeng, M.Q.; Hu, R.Z.; Song, K.Q.; Dai, L.Y.; Lu, Z.C. Enhancement of wear properties of ultrafine-structured Al–Sn alloy-embedded Sn nanoparticles through in situ synthesis. *Tribol. Lett.* **2019**, *67*, 84. [CrossRef]
13. Liu, X.; Zeng, M.Q.; Ma, Y.; Zhu, M. Promoting the high load-carrying capability of Al–20 wt% Sn bearing alloys through creating nanocomposite structure by mechanical alloying. *Wear* **2012**, *294–295*, 387–394. [CrossRef]
14. Ujah, C.O.; Kallon, D.V. Trends in aluminum matrix composite development. *Crystals* **2022**, *12*, 1357. [CrossRef]
15. Garg, P.; Jamwal, A.; Kumar, D.; Kumar Sadasivuni, K.; Mustansar Hussain, C.; Gupta, P. Advance research progresses in aluminum matrix composites: Manufacturing & applications. *J. Mater. Res. Technol.* **2019**, *8*, 4924–4939. [CrossRef]
16. Goudar, D.M.; Srivastava, V.C.; Rudrakshi, G.B.; Raju, K.; Ojha, S.N. Effect of tin on the wear properties of spray formed Al–17Si alloy. *Trans. Indian Inst. Met.* **2015**, *68*, 3–7. [CrossRef]
17. Song, K.Q.; Lu, Z.C.; Zhu, M.; Hu, R.Z.; Zeng, M.Q. A remarkable enhancement of mechanical and wear properties by creating a dual-scale structure in an Al-Sn-Si alloy. *Surf. Coat. Technol.* **2017**, *325*, 682–688. [CrossRef]
18. Rusin, N.M.; Skorentsev, A.L.; Kolubaev, E.A. Effect of equal channel angular pressing on mechanical and tribological properties of sintered Al-Sn composites. *J. Mater. Eng. Perf.* **2020**, *29*, 1955–1963. [CrossRef]
19. Rusin, N.M.; Skorentsev, A.L.; Krinitcyn, M.G.; Dmitriev, A.I. Tribotechnical properties of sintered antifriction aluminum-based composite under dry friction against steel. *Materials* **2022**, *15*, 108. [CrossRef]
20. Raghukiran, N.; Kumar, R. Processing and dry sliding wear performance of spray deposited hyper-eutectic aluminum-silicon alloys. *J. Mater. Process. Technol.* **2013**, *213*, 401–410. [CrossRef]
21. Ayyanar, S.; Gnanavelbabu, A.; Rajkumar, K.; Loganathan, P. Studies on high temperature wear and friction behaviour of AA6061/B4C/hBN hybrid composites. *Met. Mater. Int.* **2021**, *27*, 3040–3057. [CrossRef]
22. Jiao, L.; Li, F.; Zhao, Y.; Wang, B.; Huang, X.; Li, H.; Wu, T.; Cao, L. Surface friction and wear behavior of in situ AlB2 particle-reinforced A356 composites. *J. Mater. Eng. Perf.* **2022**, *31*, 5812–5822. [CrossRef]
23. Selvakumar, V.; Muruganandam, S.; Senthilkumar, N. Evaluation of mechanical and tribological behavior of Al–4% Cu–x% SiC composites prepared through powder metallurgy technique. *Trans. Indian Inst. Met.* **2017**, *70*, 1305–1315. [CrossRef]
24. Rusin, N.M.; Skorentsev, A.L. Tribological properties of sintered Al–Sn alloy doped with iron. *J. Frict. Wear* **2022**, *43*, 153–159. [CrossRef]
25. Liu, Y.; Yin, F.; Hu, J.; Li, Z.; Cheng, S. Phase equilibria of Al–Fe–Sn ternary system. *Trans. Nonferr. Met. Soc. China.* **2018**, *28*, 282–289. [CrossRef]
26. Rusin, N.M.; Skorentsev, A.L. Mechanical and tribological properties of sintered aluminum matrix Al–Sn composites reinforced with Al_3Fe particles. *Phys. Metals Metallogr.* **2021**, *122*, 1248–1255. [CrossRef]
27. Schaffer, G.B.; Sercombe, T.B.; Lumley, R.N. Liquid phase sintering of aluminium alloys. *Mater. Chem. Phys.* **2001**, *67*, 85–91. [CrossRef]
28. Ma, C.H.; Swalin, R.A. A study of solute diffusion in liquid tin. *Acta Metall.* **1960**, *8*, 388–395. [CrossRef]
29. Savitskii, A.P. Liquid Phase Sintering of the Systems with Interacting Components. In *Advanced Science and Technology of Sintering*; Stojanović, B.D., Skorokhod, V.V., Nikolić, M.V., Eds.; Kluwer Academic Plenum Publishers: New York, NY, USA, 1999.
30. Romanov, G.N. Liquid-phase sintering of aluminum-based powder alloys. *Russ. J. Non-Ferr. Met.* **2010**, *51*, 347–351. [CrossRef]

Disclaimer/Publisher's Note: The statements, opinions and data contained in all publications are solely those of the individual author(s) and contributor(s) and not of MDPI and/or the editor(s). MDPI and/or the editor(s) disclaim responsibility for any injury to people or property resulting from any ideas, methods, instructions or products referred to in the content.